



Compact and low loss 90° optical hybrid on a silicon-on-insulator platform

HANG GUAN,^{1,2,3,*} YANGJIN MA,^{1,3} RUIZHI SHI,¹ XIAOLIANG ZHU,¹ RICK YOUNCE,¹ YAOJIA CHEN,¹ JOSE ROMAN,¹ NOAM OPHIR,¹ YANG LIU,¹ RAN DING,¹ THOMAS BAEHR-JONES,¹ KEREN BERGMAN,² AND MICHAEL HOCHBERG¹

¹Elenion Technologies, New York, NY 10016, USA

²Department of Electrical Engineering, Columbia University, New York, NY 10027, USA

³These authors contributed equally

*hg2388@columbia.edu

Abstract: We present a compact and low loss 90° optical hybrid on a silicon-on-insulator (SOI) platform for coherent receiving systems. Our 90° optical hybrid uses a novel topology, comprising one Y-junction and three 2x2 multimode interference (MMI) couplers. The geometry of the 90° optical hybrid is fully optimized using particle swarm optimization (PSO). The fabricated 90° optical hybrid has a compact footprint of 21.6 μm x 27.9 μm, with an insertion loss less than 0.5 dB, a common mode rejection ratio (CMRR) larger than 30 dB, and phase error smaller than 3° in the C-band across 22 reticles on one wafer. The measured phase error (< 3°) in a packaged coherent receiver further confirms the excellent performance of the 90° optical hybrid.

© 2017 Optical Society of America

OCIS codes: (060.1660) Coherent communications; (230.3120) Integrated optics devices; (230.7370) Waveguides.

References and links

1. R. W. Tkach, "Scaling optical communications for the next decade and beyond," *Bell Labs Tech. J.* **14**(4), 3–9 (2010).
2. M. Nakazawa, K. Kikuchi, and T. Miyazaki, *High Spectral Density Optical Communication Technologies* (Springer, 2010).
3. P. Dong, X. Liu, S. Chandrasekhar, L. Buhl, R. Aroca, and Y.-K. Chen, "Monolithic silicon photonic integrated circuits for compact 100+ Gb/s coherent optical receivers and transmitters," *IEEE J. Sel. Top. Quantum Electron.* **20**(4), 150–157 (2014).
4. K. Kikuchi, "Fundamentals of coherent optical fiber communications," *J. Lightwave Technol.* **34**(1), 157–179 (2016).
5. C. Lam, H. Liu, B. Koley, X. Zhao, V. Kamalov, and V. Gill, "Fiber optic communication technologies: what's needed for datacenter network operations," *IEEE Commun. Mag.* **48**(7), 32–39 (2010).
6. H. Rohde, E. Gottwald, A. Teixeira, J. D. Reis, A. Shahpari, K. Pulverer, and J. S. Wey, "Coherent ultra dense WDM technology for next generation optical metro and access networks," *J. Lightwave Technol.* **32**(10), 2041–2052 (2014).
7. E. Agrell, M. Karlsson, A. R. Chraplyvy, D. J. Richardson, P. M. Krumrich, P. Winzer, K. Roberts, J. K. Fisher, S. J. Savory, B. J. Eggleton, M. Secondini, F. R. Kschischang, A. Lord, J. Prat, I. Tomkos, J. E. Bowers, S. Srinivasan, M. B. Pearce, and N. Gisin, "Roadmap of optical communications," *J. Opt.* **18**(6), 063002 (2016).
8. K. N. Nguyen, P. J. Skahan, J. M. Garcia, E. Lively, H. N. Poulsen, D. M. Baney, and D. J. Blumenthal, "Monolithically integrated dual-quadrature receiver on InP with 30 nm tunable local oscillator," *Opt. Express* **19**(26), B716–B721 (2011).
9. Y. Sakamaki, H. Yamazaki, T. Mizuno, T. Goh, Y. Nasu, T. Hashimoto, S. Kamei, K. Hattori, and H. Takahashi, "One-chip integrated dual polarization optical hybrid using silica-based planar lightwave circuit technology," in *European Conference and Exhibition on Optical Communication* (IEEE, 2009), pp. 1–2.
10. F. Gambini, G. Meloni, S. Faralli, G. Contestabile, L. Poti, and J. Klamkin, "Ultra-compact 56-Gb/s QPSK and 80-Gb/s 16-QAM silicon coherent receiver free of waveguide crossings," in *Proceedings of IEEE Conference on Group IV Photonics* (IEEE, 2014), pp. 149–150.
11. S. Faralli, G. Meloni, F. Gambini, J. Klamkin, L. Poti, and G. Contestabile, "A compact silicon coherent receiver without waveguide crossing," *IEEE Photonics J.* **7**(4), 1–6 (2015).
12. K. Voigt, L. Zimmermann, G. Winzer, H. Tian, B. Tillack, and K. Petermann, "C-band optical 90° hybrids in silicon nanowaveguide technology," *IEEE Photonics Technol. Lett.* **23**(23), 1769–1771 (2011).

13. P. Runge, S. Schubert, A. Seeger, K. Janiak, J. Stephan, D. Trommer, P. Domburg, and M. L. Nielsen, "Monolithic InP receiver chip with a 90° hybrid and 56 GHz balanced photodiodes," *Opt. Express* **20**(26), B250–B255 (2012).
14. S.-H. Jeong and K. Morito, "Novel optical 90° hybrid consisting of a paired interference based 2×4 MMI coupler, a phase shifter and a 2×2 MMI Coupler," *J. Lightwave Technol.* **28**(9), 1323–1331 (2010).
15. W. Yang, M. Yin, Y. Li, X. Wang, and Z. Wang, "Ultra-compact optical 90° hybrid based on a wedge-shaped 2 × 4 MMI coupler and a 2 × 2 MMI coupler in silicon-on-insulator," *Opt. Express* **21**(23), 28423–28431 (2013).
16. H. Yagi, N. Inoue, R. Masuyama, T. Kikuchi, T. Katsuyama, Y. Tateiwa, K. Uesaka, Y. Yoneda, M. Takechi, and H. Shoji, "InP-Based pin-Photodiode Array Integrated With 90° Hybrid Using Butt-Joint Regrowth for Compact 100 Gb/s Coherent Receiver," *IEEE J. Sel. Top. Quantum Electron.* **20**(6), 374–380 (2014).
17. Y. Sakamaki, T. Kawai, T. Komukai, M. Fukutoku, T. Kataoka, T. Watanabe, and Y. Ishii, "Experimental demonstration of multi-degree colorless, directionless, contentionless ROADM for 127-Gbit/s PDM-QPSK transmission system," *Opt. Express* **19**(26), B1–B11 (2011).
18. D. Hoffman, H. Heidrich, G. Wenke, R. Langenhorst, and E. Dietrich, "Integrated optics eight-port 90° hybrid on LiNbO₃," *J. Lightwave Technol.* **7**(5), 794–798 (1989).
19. M. Seimetz and C. M. Weinert, "Options, feasibility and availability of 2×4 90° hybrids for coherent optical systems," *J. Lightwave Technol.* **24**(3), 1317–1322 (2006).
20. S. Jeong and K. Morito, "Simple analytical calculation and experimental demonstration of optical 90° hybrids based on tapered 2×4 and 2×2 multimode interference couplers," *J. Opt. Soc. Am. B* **28**(1), 159–164 (2011).
21. R. Halir, G. Roelkens, A. Ortega-Moñux, and J. G. Wangüemert-Pérez, "High-performance 90° hybrid based on a silicon-on-insulator multimode interference coupler," *Opt. Lett.* **36**(2), 178–180 (2011).
22. M. Bachmann, P. A. Besse, and H. Melchior, "General self-imaging properties in N × N multimode interference couplers including phase relations," *Appl. Opt.* **33**(18), 3905–3911 (1994).
23. L. B. Soldano and C. M. Pennings, "Optical multi-mode interference devices based on self-imaging: Principles and Applications," *J. Lightwave Technol.* **13**(4), 615–627 (1995).
24. M. R. Paiam and R. I. Macdonald, "Design of phased-array wavelength division multiplexers using multimode interference couplers," *Appl. Opt.* **36**(21), 5097–5108 (1997).
25. R. Adar, C. H. Henry, M. A. Milbrodt, and R. C. Kistler, "Phase coherence of optical waveguides," *J. Lightwave Technol.* **12**(4), 603–606 (1994).
26. Y. Yang, Y. Ma, H. Guan, Y. Liu, S. Danziger, S. Ocheltree, K. Bergman, T. Baehr-Jones, and M. Hochberg, "Phase coherence length in silicon photonic platform," *Opt. Express* **23**(13), 16890–16902 (2015).
27. L. Chrostowski, X. Wang, J. Flueckiger, Y. Wu, Y. Wang, and S. T. Fard, "Impact of fabrication non-uniformity on chip-scale silicon photonic integrated circuits," in *Optical Fiber Communication Conference* (OSA, 2014), paper Th2A37.
28. Y. Zhang, S. Yang, A. E.-J. Lim, G.-Q. Lo, C. Galland, T. Baehr-Jones, and M. Hochberg, "A compact and low loss Y-junction for submicron silicon waveguide," *Opt. Express* **21**(1), 1310–1316 (2013).
29. Y. Ma, Y. Zhang, S. Yang, A. Novack, R. Ding, A. E.-J. Lim, G.-Q. Lo, T. Baehr-Jones, and M. Hochberg, "Ultralow loss single layer submicron silicon waveguide crossing for SOI optical interconnect," *Opt. Express* **21**(24), 29374–29382 (2013).
30. H. Guan, Y. Ma, R. Shi, A. Novack, J. Tao, Q. Fang, A. E.-J. Lim, G.-Q. Lo, T. Baehr-Jones, and M. Hochberg, "Ultracompact silicon-on-insulator polarization rotator for polarization-diversified circuits," *Opt. Lett.* **39**(16), 4703–4706 (2014).
31. Y. Vlasov and S. McNab, "Losses in single-mode silicon-on-insulator strip waveguides and bends," *Opt. Express* **12**(8), 1622–1631 (2004).
32. W. Bogaerts and S. K. Selvaraja, "Compact single-mode silicon hybrid rib/strip waveguide with adiabatic bends," *IEEE Photonics J.* **3**(3), 422–432 (2011).
33. T. Fujisawa, S. Makino, T. Sato, and K. Saitoh, "Low-loss, compact, and fabrication-tolerant Si-wire 90° waveguide bend using clothoid and normal curves for large scale photonic integrated circuits," *Opt. Express* **25**(8), 9150–9159 (2017).
34. A. Novack, Y. Liu, R. Ding, M. Gould, T. Baehr-Jones, Q. Li, Y. Yang, Y. Ma, Y. Zhang, K. Padmaraju, K. Bergman, A. E.-J. Lim, G.-Q. Lo, and M. Hochberg, "A 30 GHz silicon photonic platform," in *Proceedings of IEEE Conference on Group IV Photonics* (IEEE, 2013), pp. 7–8.
35. "Implementation Agreement for CFP2-Analogue Coherent Optics Module," OIF.2014.75.13, Working Group: PLL, October 2013.

1. Introduction

The rapid growth of data transmission capacity has driven the development of optical transmission systems with high spectral efficiency, high channel data rate, and low cost [1,2]. To economically extend the reach and data capacity of next-generation networks, coherent optical communication technologies using modulation formats like quadrature phase shift keyed (QPSK) modulation and quadrature amplitude modulation (QAM) have been widely deployed in long-haul networks [3,4]. Compared to traditional transmission systems, coherent optical transmission systems offer better spectral efficiency and receiver sensitivity as well as

better tolerance to amplitude spontaneous emission (ASE) noise, chromatic dispersion, and polarization mode dispersion (PMD) [5]. In addition to their use in long-haul networks, coherent transmission technologies are also being used in metro networks where traffic loads require use of transceivers on a much larger scale [6,7].

A 90° optical hybrid is a key component in coherent transmission systems. It mixes the incoming signal with the four quadrature states associated with the reference signal (LO) in the complex-field space and then delivers the four light signals to two pairs of balanced detectors. There are two major types of 90° optical hybrids: Type-I is based on several discrete components such as 1x2 couplers, 2x2 couplers and phase shifters [8–11]; Type-II is based on a single device such as a 4x4 multimode interference (MMI) coupler [12,13]. There are designs constructed by 2x4 MMI couplers followed by 2x2 MMI couplers [14–16], which can be regarded as a derivative of Type-II hybrid.

Type-I hybrids have been demonstrated in silica-based planar lightwave circuits [9,17] and LiNbO₃-based integrated circuits [18]. Recently, Type-I hybrids which avert waveguide crossing to mitigate crosstalk have been demonstrated on a silicon-on-insulator (SOI) platform [10,11]. These designs require accurate control of phase in the waveguides [19], a feature which is difficult to achieve in high-index-contrast photonics platforms due to waveguide sidewall roughness and thickness variations. Thermal phase shifters can be implemented to tune the phase to the desired value [8], but this design creates complexities for control of real systems.

Type-II hybrids are generally the solution of choice in high-index-contrast platforms like deeply-etched indium phosphide (InP) [13,14,20] and silicon-on-insulator [12,15,21] because they are fully passive and require no active control loop to stabilize the 90° phase relation. However, governed by the self-imaging theory [22–24], to realize optimum self-imaging, 90° optical hybrids based on 4x4 MMI couplers or 2x4 MMI couplers usually have a length of hundreds of micrometers. This requirement not only hinders the further scaling-down of the footprint, but more importantly it results in low-quality imaging because of the strong phase errors of the higher-order modes [21]. Due to mode dispersion, it is difficult for Type-II hybrids to achieve broadband self-imaging. Therefore, loss and phase error in Type-II hybrids exhibit strong wavelength dependence and process dependence. For commercial purposes, the critical parameter is usually not the performance at the best wavelength, but performance at the worst wavelength, therefore making it very challenging to meet the tight requirements for high-order QAM.

We present a compact 90° optical hybrid that achieves a footprint of 21.6 μm x 27.9 μm. To the best of our knowledge, this optical hybrid has the most compact size among all the waveguide-based 90° optical hybrids that have already been reported. The 90° optical hybrid adopts a novel topology that consists of one Y-junction, three 2x2 MMI couplers, and four 90° bends. It is a derivative of Type-I hybrids, but it is unique because it is purely passive with a topological layout that can be easily applied on all integrated photonics platforms. The topology of our 90° optical hybrid is fully optimized using particle swarm optimization (PSO) to achieve low insertion loss (< 0.5 dB), low phase error (< 3°), and high common mode rejection ratio (CMRR > 30 dB).

The remainder of the paper is organized as follows: The performance of the 90° optical hybrid is first investigated by analytical analysis and then optimized in a 3-D finite-difference time-domain (FDTD) simulation environment using particle swarm optimization. Thereafter, the fabricated 90° optical hybrid is characterized across a whole wafer and in packaged coherent receivers. Finally, we benchmark our work against previous works and conclude our discussions.

2. Design and fabrication

2.1 Device structure

Figure 1 shows the schematic diagram of the proposed 90° optical hybrid which consists of one Y-junction and three 2x2 MMI couplers connected by four identical 90° bends. The signal and local oscillator (LO) inputs come from the bottom 2x2 MMI coupler and the top Y-junction. The quadrature channels (Q) are the outputs of the left 2x2 MMI couplers, and the in-phase channels (I) are the outputs of the right 2x2 MMI couplers. Note that 2x2 MMI couplers in the schematic diagram can be replaced with other types of 2x2 couplers like 3-dB directional couplers.

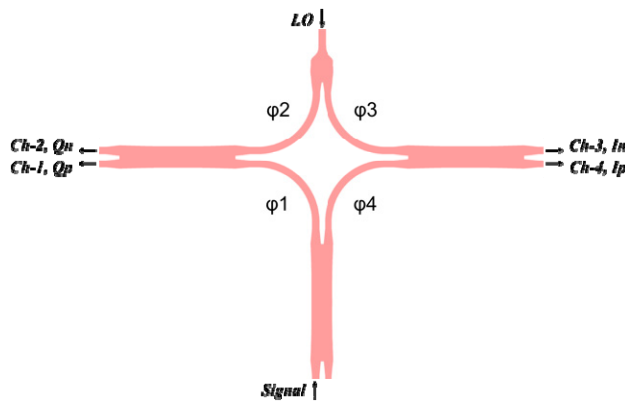


Fig. 1. Schematic diagram of the proposed 90° optical hybrid.

The quadrature phase behavior of the 90° optical hybrid can be analytically described as follows: If we set the electric field of the signal (E_S) and the LO (E_{LO}) to be the input of the bottom 2x2 MMI coupler and the input of the Y-junction, then the output fields of the 90° optical hybrid are represented by

$$\begin{bmatrix} E_1 \\ E_2 \\ E_3 \\ E_4 \end{bmatrix} = [T_3] \cdot [T_2] \cdot [T_1] \cdot \begin{bmatrix} E_S \\ E_{LO} \\ 0 \\ 0 \end{bmatrix} \quad (1)$$

In Eq. (1), $[T_1]$ indicates the transfer matrix for the Y-junction and the bottom 2x2 MMI coupler. $[T_2]$ is the transfer matrix for the four 90° bends, and $[T_3]$ is the transfer matrix of the left and right 2x2 MMI couplers.

$$[T_1] = \sqrt{\kappa} \cdot \begin{bmatrix} 1 & 0 & 0 & 0 \\ 0 & 1 & 0 & 0 \\ 0 & 0 & 1 & 0 \\ e^{j\theta} & 0 & 0 & 0 \end{bmatrix} \quad (2)$$

$$[T_2] = \begin{bmatrix} e^{j\varphi_1} & 0 & 0 & 0 \\ 0 & e^{j\varphi_2} & 0 & 0 \\ 0 & 0 & e^{j\varphi_3} & 0 \\ 0 & 0 & 0 & e^{j\varphi_4} \end{bmatrix} \quad (3)$$

$$[T_3] = \sqrt{\kappa} \cdot \begin{bmatrix} 1 & e^{j\theta} & 0 & 0 \\ e^{j\theta} & 1 & 0 & 0 \\ 0 & 0 & 1 & e^{j\theta} \\ 0 & 0 & e^{j\theta} & 1 \end{bmatrix} \quad (4)$$

where κ indicates a power splitting coefficient of the 2x2 MMI coupler and θ is the phase shift introduced by the 2x2 MMI coupler. φ_1 , φ_2 , φ_3 , and φ_4 are the phase shifts introduced by the four bends. By plugging Eqs. (2)-(4) into Eq. (1), we have Eq. (5)

$$\begin{bmatrix} E_1 \\ E_2 \\ E_3 \\ E_4 \end{bmatrix} = \kappa \cdot \begin{bmatrix} e^{j\varphi_1} E_S + e^{j(\theta+\varphi_2)} E_{LO} \\ e^{j(\theta+\varphi_1)} E_S + e^{j\varphi_2} E_{LO} \\ e^{j(2\theta+\varphi_4)} E_S + e^{j\varphi_3} E_{LO} \\ e^{j(\theta+\varphi_4)} E_S + e^{j(\theta+\varphi_3)} E_{LO} \end{bmatrix} \quad (5)$$

We now separate our discussion into two different cases – an ideal case and a realistic case. In the ideal case, we assume perfect phase shift of the 2x2 MMI couplers ($\theta = \pi/2$) and the phase shifts introduced by the 90° bends satisfy the condition given by Eq. (6)

$$\varphi_1 = \varphi_4 \text{ and } \varphi_2 = \varphi_3 \quad (6)$$

If we further consider perfect power balance ($\kappa = 1/2$) and ignore any constant phase offset, then Eq. (5) can be simplified to Eq. (7). Since the phase relation at the outputs is rotated by 90° relative to each other, the proposed scheme works as a 90° optical hybrid.

$$\begin{bmatrix} E_1 \\ E_2 \\ E_3 \\ E_4 \end{bmatrix} = \frac{1}{2} \cdot \begin{bmatrix} E_S + jE_{LO} \\ E_S - jE_{LO} \\ E_S - E_{LO} \\ E_S + E_{LO} \end{bmatrix} \quad (7)$$

In the realistic case, the assumptions above about the phase shifts of the 2x2 MMI couplers and the 90° bends do not hold because of variation in fabrication. Phase error of the proposed 90° optical hybrid is defined as the phase difference deviation from 90° given by Eq. (8).

$$\text{phase_error} = \frac{\pi}{2} - (\varphi_2 - \varphi_1) - (\varphi_4 - \varphi_3) - \theta \quad (8)$$

Phase error of the proposed 90° optical hybrid comes from two sources: 2x2 MMI coupler phase uncertainties and waveguide phase uncertainties. Phase uncertainties in a high index contrast Si waveguide comes from all kinds of non-idealities in fabrication, to name a few: non-uniform waveguide width due to lithography, waveguide sidewall roughness, and SOI wafer thickness variation. The phase error of 2x2 MMI coupler is within 1.2° based on our simulations as shown in Fig. 2(d). The phase error from the four 90° bends can be estimated using coherence length theory [25]. Coherence length of two uncorrelated waveguides was reported ~4 mm in a silicon photonics platform with 248 nm lithography [26]. If we assume the total length in bent waveguide routing is 25 μm (corresponds to ~4 μm bend radius), phase uncertainty is estimated to be 6.4°. This estimation defines a guideline in design since phase coherence length strongly depends on the fabrication process and the distance between two waveguides [27]. Based on this analysis, we chose 4 μm bend radius for the proposed 90° optical hybrid. As demonstrated in Section 3, the measured phase error of the 90° optical hybrid is below 3° in the C band, which to the best of our knowledge is the smallest phase error that has been reported so far.

Other important figures of merit of a 90° optical hybrid are defined as follows. Note that these parameters have the same definition for both signal input and LO input.

1. Insertion loss is defined as the input power subtracted by the sum of power from the four output ports as given in Eq. (9)

$$Loss = 10 \cdot \log(P_{Input}) - \sum 10 \cdot \log(P_i) \quad i = I_p, I_n, Q_p, Q_n \quad (9)$$

2. Common mode rejection ratio (CMRR) is given in Eq. (10)

$$\begin{aligned} CMRR_I &= 20 \cdot \log\left(\frac{|P_{I_p} - P_{I_n}|}{|P_{I_p} + P_{I_n}|}\right) \\ CMRR_Q &= 20 \cdot \log\left(\frac{|P_{Q_p} - P_{Q_n}|}{|P_{Q_p} + P_{Q_n}|}\right) \end{aligned} \quad (10)$$

3. Imbalance is defined as the subtraction between the power of the positive and negative ports as given in Eq. (11)

$$\begin{aligned} Imbalance_I &= 10 \cdot \log\left(\frac{P_{I_p}}{P_{I_n}}\right) \\ Imbalance_Q &= 10 \cdot \log\left(\frac{P_{Q_p}}{P_{Q_n}}\right) \end{aligned} \quad (11)$$

2.2 Device optimization

The goal is to find the optimum geometry of the proposed 90° optical hybrid that can achieve low insertion loss, low phase error, and high CMRR with a compact device footprint. To meet this goal, we adopt PSO which has been widely used in designing compact and high-performance passive devices [28–30].

The design of our 90° optical hybrid is a two-step process. In the first step, we design and optimize all three subcomponents, including the Y-junction, the 90° bend, and the 2x2 MMI couplers, individually. For the Y-junction, we use an improved design of our previous work [28] with excess loss < 0.1dB across C-band. For the 90° bends, we use the normal 90° bends with bend radii of 4 μm. The typical loss of a small radius 90° bend is on the order of 0.01 dB [31], a sufficiently low loss for our application. Although ultralow loss 90° bends [32,33] exist and are preferred for large-scale photonic integrated circuits, they are not mandated for our individual 90° optical hybrid.

Traditional 2x2 MMI coupler has a rectangular shape. Design freedom is thus limited to the width and the length of the MMI coupler. The traditional 2x2 MMI coupler suffers from high scattering loss at the input/output ports and high output power imbalance due to imperfect self-imaging. Here we introduce the design methodology of a compact, low-loss, and low-imbalance 2x2 MMI coupler by breaking the rectangular geometry constraint.

Figure 2(a) illustrates a schematic diagram of the 2x2 MMI coupler, that is symmetric to both the x-axis and the y-axis. Four tapers provide adiabatic transition between the interconnecting waveguide (W_4) and the MMI access waveguides (W_5) to further reduce mode mismatching loss. W_6 is the gap between two tapers with W_3 equal to $2W_5 + W_6$. The multimode region is digitalized into 4 segments with interpolations between each segment. W_1 , W_2 , W_3 , L_2 , and L_3 are optimized to yield the minimum imbalance and insertion loss. The optimization figure of merit (FOM) is in Eq. (12) as

$$FOM = \sum (0.5 - y_1(\lambda))^2 + \sum (0.5 - y_2(\lambda))^2 + \sum (y_1(\lambda) - y_2(\lambda))^2 \quad (12)$$

where $y_1(\lambda)$ and $y_2(\lambda)$ correspond to the normalized optical power at the through port and cross port of the 2x2 MMI coupler. The PSO optimization is run in Lumerical 3-D FDTD.

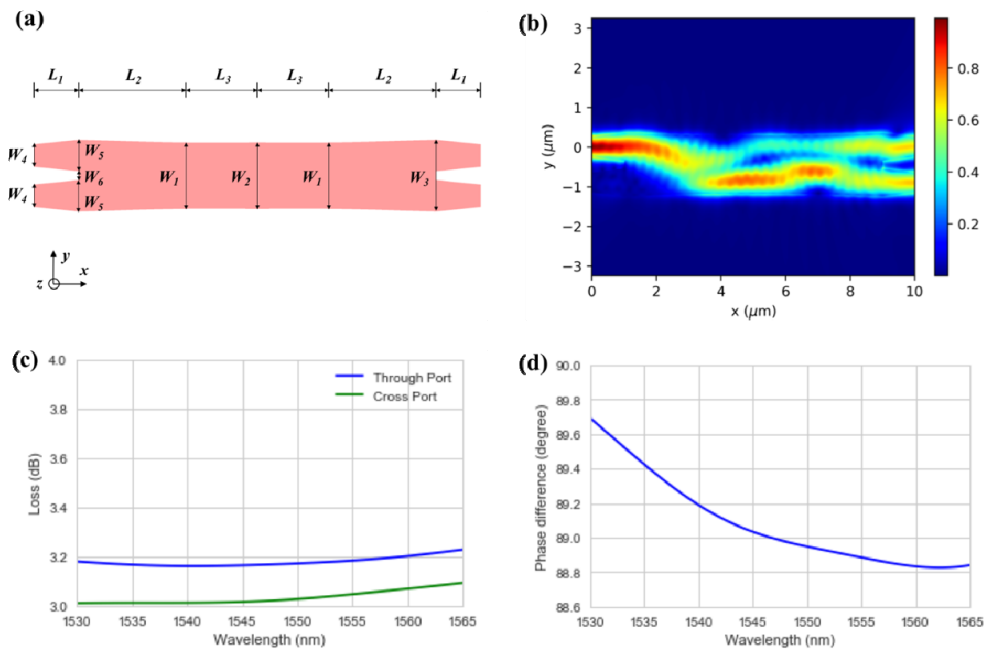


Fig. 2. (a) Schematic of the 2x2 MMI coupler (top view). The 2x2 MMI geometry is defined by cubic interpolation of W_1 to W_3 . (b) Simulated power distribution at 1550 nm wavelength. (c) Simulated 2x2 MMI coupler insertion loss. (d) Simulated 2x2 MMI coupler phase difference between the through port and the cross port.

The resulting dimensions are listed in Table 1. The top-view of the simulated electric field is shown in Fig. 2(b). Figure 2(c) shows insertion loss of the through port and cross port as a function of wavelength. Note that the intrinsic 3 dB loss for each port has not been deducted. Figure 2(d) shows the phase error is less than 1.2 ° in the C band.

Table 1. 2x2 MMI geometric parameters in μm

W_1	W_2	W_3	W_4	W_5	W_6	L_1	L_2	L_3
1.48	1.48	1.6	0.5	0.7	0.2	1	2.4	1.6

In the second step, with all the subcomponents ready, the design of the 90° optical hybrid is straightforward, that is to connect them together following the topology in Fig. 1. We verify the performance of the 90° optical hybrid using 3-D FDTD simulation. Figures 3(a) and 3(b) are the top-views of mode propagation through the 90° optical hybrid when input from the signal port and LO port, respectively. Figure 3(c) shows the total insertion loss (the sum of losses from all four output ports) as a function of wavelength. The total insertion loss is less than 0.3 dB when input is from the LO port, and less than 0.45 dB when input is from the signal port. An excellent CMRR of 30 dB is achieved for both the LO port and signal port in the C-band.

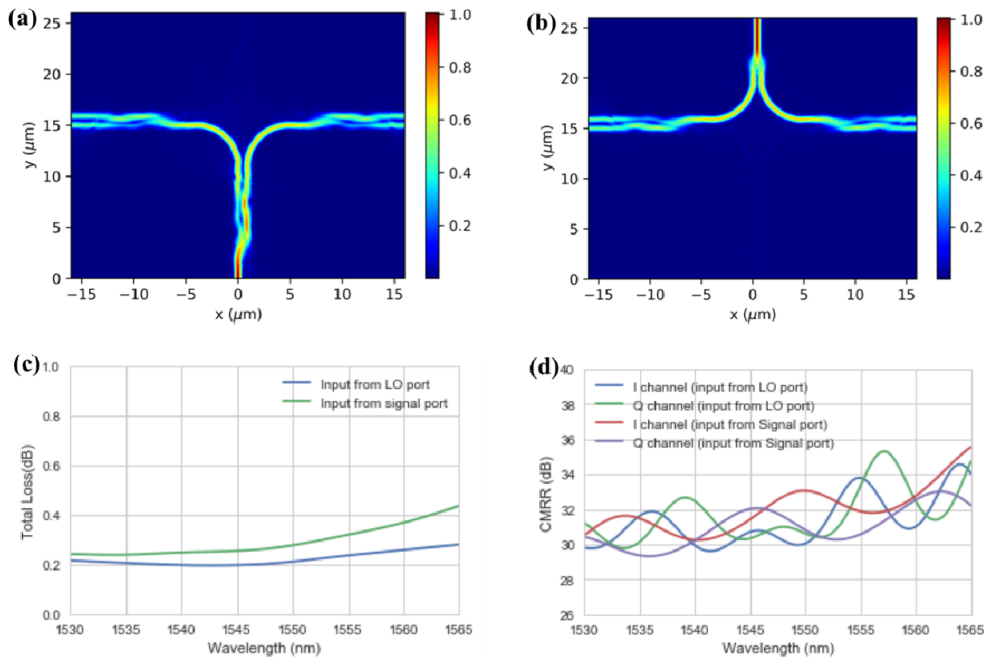


Fig. 3. Simulated E-field distribution at 1550 nm wavelength (a) when input from the signal port, (b) when input from the LO port. (c) Simulated total insertion loss. (d) Simulated CMRR.

2.3 Device fabrication

The device is fabricated in a 220-nm SOI platform [34]. Figure 4(a) shows an optical image of the fabricated 90° optical hybrid. We implemented two kinds of test structures to characterize different performance metrics of the 90° optical hybrid. One kind of test structure has a Mach-Zehnder (MZ) delay interferometer with a length difference of 126 μm before the 90° optical hybrid used to extract phase error [14,15]. The four outputs of the 90° optical hybrid are connected directly to grating couplers. The other kind of test structure does not have an MZ delay interferometer. Its LO and signal inputs are connected directly to the grating coupler array, and its outputs are connected to photodetectors (PDs) to extract loss and CMRR.

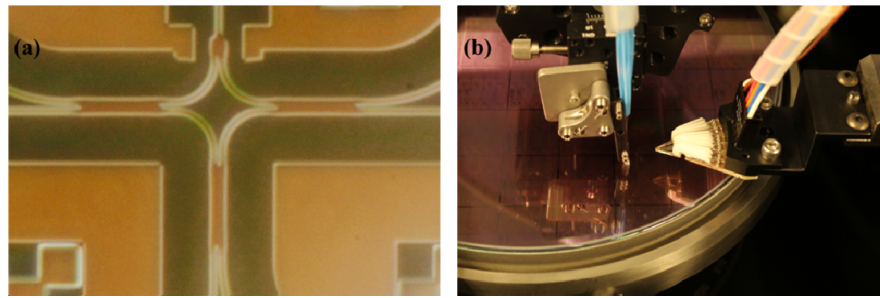


Fig. 4. (a) Optical image of the fabricated 90° optical hybrid, and (b) Image of the automatic wafer-level test setup.

3. Measurement and discussion

3.1 Measurement results across one wafer

The device is measured in an automated wafer-level test setup as shown in Fig. 4(b). Light from a tunable laser was coupled into the test structure via a polarization maintaining (PM) fiber array and grating couplers (GCs). Depending on the type of test structure, the outputs of the 90° optical hybrid came out either through the same PM fiber array and were measured using an optical power meter to extract the phase error or through a DC probe and were measured using source meters to extract loss and CMRR. In the phase error measurement, phase error extracted from MZ delay interferometer spectrum does not depend on the absolute GC loss nor GC center wavelength. In the loss and CMRR measurement, the on-chip light after GC is first split by a Y-junction with a 50:50 splitting ratio. One branch of the Y-junction goes into the LO/signal port of the hybrid. The four output ports of the hybrid are connected to four on-chip photodetectors. The other branch of the Y-junction goes into another on-chip photodetector for calibration. We extracted the loss and CMRR of the hybrid by subtracting the photocurrents from the four photodetectors to that from the calibration photodetector. In both cases, variation of GC does not propagate into the measurement.

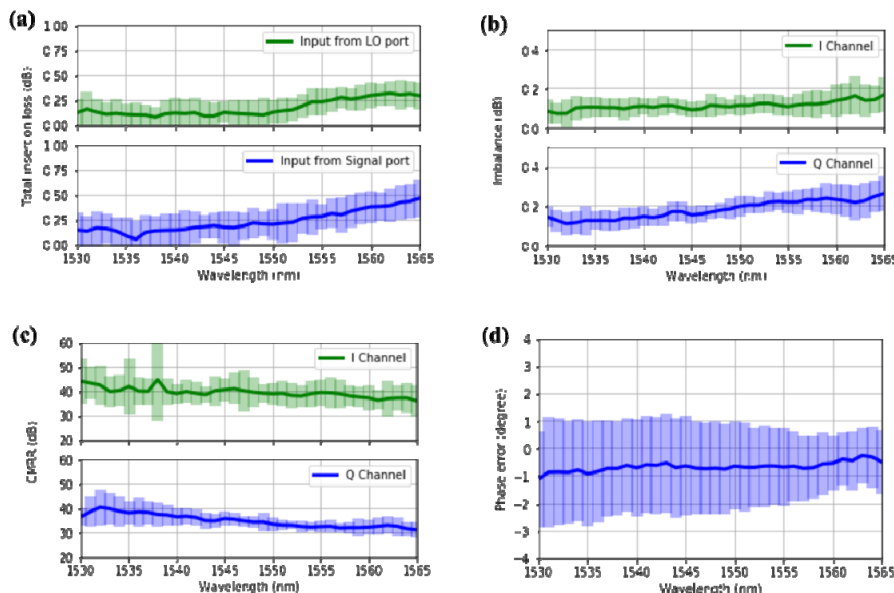


Fig. 5. Measured (a) total insertion loss, (b) imbalance, (c) CMRR, and (d) phase error of the 90° optical hybrid (dark curve is the averaged value over 22 dies, and light-colored region indicates the 1- δ deviation).

To verify the uniformity of the 90° optical hybrid after fabrication, we run automated tests on 22 dies across one 8-inch wafer. To the best of our knowledge, this is the first time that the statistics of the fabricated 90° optical hybrid have been reported. Figure 5(a) shows the measured total insertion loss of the 90° optical hybrids. The solid lines are the averaged total insertion loss over 22 dies, and the light-colored bars represent the 1- δ deviation (68.27% data values are within 1- δ deviation of the averaged value). The averaged loss is less than 0.5 dB for both signal and LO inputs in the entire C band. Even considering 1- δ deviation, the worst-case insertion loss is less than 0.6 dB. Figure 5(b) illustrates the measured imbalance of both the in-phase channel and the quadrature channel. The averaged imbalance is better than 0.25 dB in the C-band. When considering the 1- δ deviation, the worst-case power imbalance is less than 0.35 dB. Figure 5(c) shows the measured CMRR of both the in-phase channel and the quadrature channel. The averaged CMRR is larger than 31 dB in the C-band. Even

considering $1-\delta$ deviation, the worst-case CMRR is larger than 28 dB. Figure 5(d) shows the measured phase error. The averaged phase error is within 0° to -1° . The $1-\delta$ phase error deviation falls between -3° to 3° , indicating the excellent phase controllability of the 90° optical hybrids.

Figure 6 shows the measured performance of the 90° optical hybrid in a single die. We see that the 90° optical hybrid achieves an insertion loss of less than 0.45 dB, with phase errors smaller than 2° and CMRR larger than 30 dB over the C band.

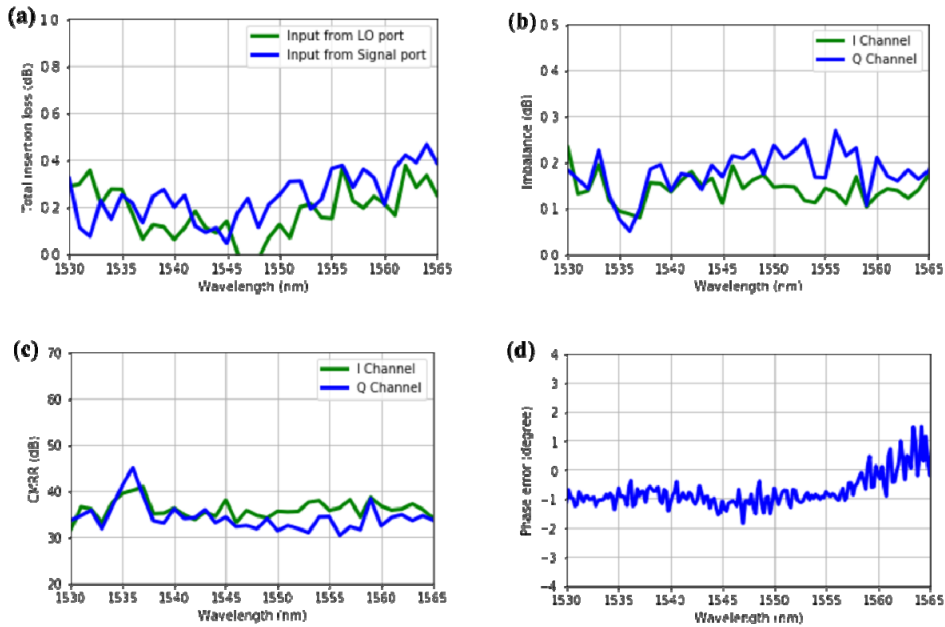


Fig. 6. Measured (a) total insertion loss, (b) imbalance, (c) CMRR, and (d) phase error of the 90° optical hybrid in a typical die.

3.2 Measurement results of packaged coherent receivers

Figure 7(a) shows the schematic diagram of a packaged coherent receiver. To measure the phase error of the packaged coherent receiver, light at two different frequencies is shined into the signal and LO ports respectively. These two frequencies beat in the 90° optical hybrid and generate sinusoid waves at I and Q ports. The waves are then magnified by the trans-impedance amplifiers (TIAs) and captured by high-speed oscilloscope. Figure 7(b) shows the measured voltages of the I and Q ports.

Phase difference between I and Q ports [35] is then calculated in the time domain at different frequency offsets as shown in Fig. 7(c). The dots indicate the measured phase difference at different frequency offsets, and the solid line is the linear fitting of the dots. Phase error is calculated by subtracting 90° by the y-intercept. Figure 7(d) shows the measured phase error over the C band. The measured phase error of the packaged coherent receiver is smaller than 3° which matches well with the measurement of the standalone device as shown in Fig. 5(d).

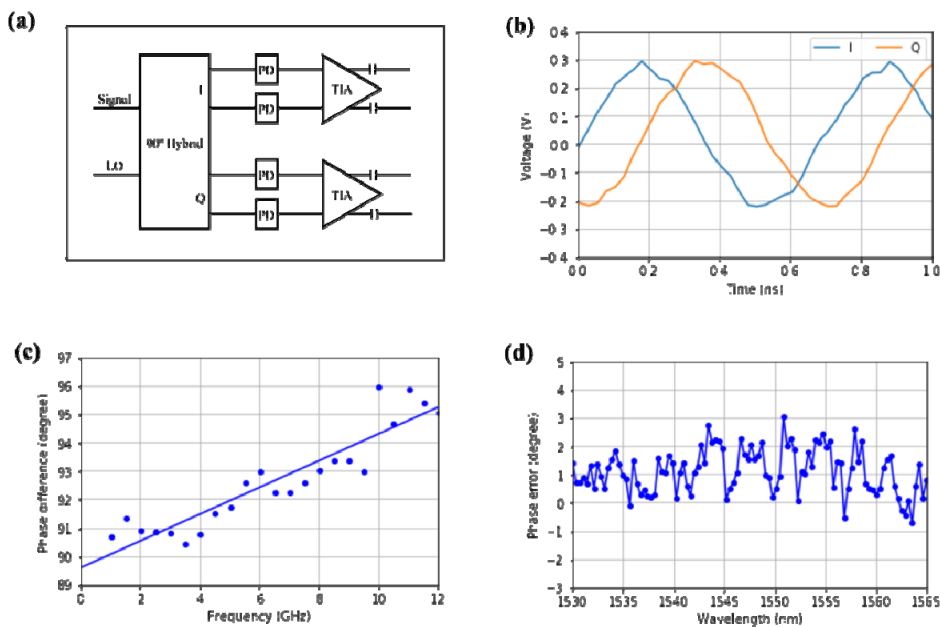


Fig. 7. (a) Schematic of the coherent receiver module. (b) Measured output voltages after TIAs as a function of time. (c) Measured phase difference between the I and Q channels as a function of beating frequency at 1550 nm. (d) Measure phase error in the entire C-band.

3.3 Discussion

The proposed 90° optical hybrid has five advantages over previous devices: (1) it does not use 2x4 MMI couplers or 4x4 MMI couplers, resulting in a drastically reduced footprint, (2) it has a lower loss, because its geometry is fully optimized using PSO, (3) it reduces the mode number and the length of the multimode region, thus reducing the phase error, (4) it does not require a waveguide crossing at the output as compared to conventional Type-I devices, thus reducing crosstalk, and (5) it is resilient to process deviation and therefore suitable for high-volume manufacturing.

To investigate the influence of the CMRR and loss of a 90° optical hybrid to the overall coherent receiver performance, we simulate the required optical signal-to-noise ratio (OSNR) to achieve a bit error rate (BER) of 2×10^{-2} in a typical coherent receiver under different CMRR and insertion loss of the 90° optical hybrid in Fig. 8. The simulation is executed in a MATLAB environment with a model of the hybrid that includes excess loss, phase error, and CMRR. Models of the transmitter and receiver are consistent with current generation transponder designs. The input is a 16-QAM dual-polarization signal at a speed of 34 Gbaud and a power of -18 dBm. The input also includes 8 adjacent channels at a power of -4.5 dBm on 50 GHz grid with 200 GHz gap to the selected channel. Note phase error within 5° can be corrected by the digital signal processor (DSP) without OSNR penalty in our simulation. Figure 8 shows that at low hybrid loss, CMRR dominates the required OSNR. For example, at a hybrid loss of 0.5 dB, the required OSNR improves ~ 4 dB when the CMRR of the hybrid improves from 20 dB to 30 dB. This result is significant because a 3-dB improvement in OSNR essentially doubles the reach of the optical channel. At a CMRR higher than 25dB, hybrid loss has more impact on OSNR but the margin of improvement is not significant.

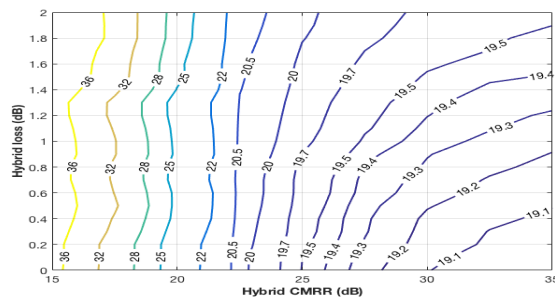


Fig. 8. Simulated required OSNR in a typical 16 QAM coherent receiver under different CMRR and insertion loss of 90° optical hybrid.

Table 2 compares the results of our work with other 90° optical hybrid works. Only our work shows measurement results of more than 20 devices across one wafer, while all other work shows only the measurement result of a single device. Loss, phase error, and CMRR are all worst-case results in C-band. Our device achieves the most compact footprint, with other metrics (loss, phase error, CMRR) better or comparable to the state-of-the-art results.

Table 2. Performance comparison of 90° optical hybrid

Property	[14] (2010)	[21] (2011)	[20] (2011)	[12] (2011)	[13] (2012)	[15] (2013)	This work ^a (Average, Best)
Material	InP	SOI	InP	SOI	InP	SOI	SOI
Type	2x4 MMI + 2x2 MMI	Shallowly- etched 4x4 MMI with two inputs	Tapered 2x4 MMI + 2x2 MMI	4x4 MMI	4x4 MMI	Wedge- shaped 2x4 MMI + 2x2MMI	PSO-optimized 2x2 MMI
Size (μm ²)	18x379 (6,822)	12x115.5 (1,386)	18.6x227.9 (4,078)	10x185 (1,850)	400x2800 (1,120,000)	12x107 (1,284)	21.6x27.9 (602)
Loss (dB)	1.5	NA	NA	0.5	NA	1	0.5, 0.45
Phase Error (°)	5	5	7	5	NA	5	3, 2
CMRR (dB)	30	15	20	20	15	20	30, 30

^aThe average column represents the measured averaged value across 22 dies, while the best column represents the measured result in a best die.

4. Conclusion

We experimentally demonstrate a 90° optical hybrid with a footprint of 21.6 μm x 27.9 μm on a SOI platform. Our hybrid consists of a Y-junction and three 2x2 MMI couplers optimized using PSO. The fabricated hybrid exhibits an insertion loss less than 0.5 dB, with phase errors smaller than 3° and CMRRs larger than 30 dB over C-band.